Numerical simulation of polarization-resolved second harmonic microscopy in birefringent media

Ivan Gusachenko, Marie-Claire Schanne-Klein

Numerical simulation of polarization-resolved second-harmonic microscopy in birefringent media

Ivan Gusachenko*

Laboratory for Optics and Biosciences, Ecole Polytechnique, Centre National de la Recherche Scientifique, Institut National de la Santé et de la Recherche Médicale U696, Palaiseau, France and Laboratory of Cellular Structure Morphology and Function, Siberian Branch of the Russian Academy of Sciences, Institute of Cytology and Genetics, Novosibirsk, Russia

Marie-Claire Schanne-Klein†

Laboratory for Optics and Biosciences, Ecole Polytechnique, Centre National de la Recherche Scientifique, Institut National de la Santé et de la Recherche Médicale U696, Palaiseau, France

(Received 5 July 2013; published 11 November 2013)

Polarization-resolved second-harmonic microscopy has recently emerged as a valuable technique for *in situ* imaging of collagen structure in tissues. Nevertheless, collagen-rich tissues such as tendon, ligament, skin dermis, bone, cornea, or artery exhibit a heterogeneous and anisotropic architecture that results in complex optical properties. While experimental evidence of polarization distortions has been reported in various tissues, the physics of second-harmonic imaging within such tissues is not fully understood yet. In this work, we performed numerical simulations of polarization-resolved second-harmonic generation in a strongly focused regime within a birefringent tissue. We show that vectorial components due to strong focusing have a rather small effect on the measurement of the second-harmonic tensorial response, while birefringence and optical dispersion may affect these measurements dramatically. We show indeed that a difference in the focal field distribution for ordinary and extraordinary waves results in different phase-matching conditions, which strongly affects the relative efficacy of second-harmonic generation for different polarizations. These results are of great interest for extracting reliable quantitative parameters from second-harmonic images.

DOI: 10.1103/PhysRevA.88.053811 PACS number(s): 42.65.Ky, 78.20.Fm, 87.64.mn, 87.85.Pq

I. INTRODUCTION

Polarization-resolved second-harmonic generation (PSHG) microscopy has recently emerged as a promising modality in nonlinear microscopy, which can probe three-dimensional structural features in biological tissues [1–15]. This technique is of great interest for studying collagen-rich tissues such as tendons, ligaments, arteries, corneas, skin dermis, and bones because fibrillar collagens exhibit strong endogenous SHG signals due to their dense noncentrosymmetrical structure [16–18]. Conventional SHG imaging relies on excitation with circularly polarized light to efficiently image collagen fibrils oriented at any angle, which is particularly relevant for collagen scoring in the context of pathological tissue remodeling [19]. In contrast, PSHG microscopy takes advantage of excitation with different polarization angles to provide additional information about the optical anisotropy inherent to fibrillar collagen in tissue.

The PSHG response from collagen is usually described by the SHG anisotropy parameter ρ, which reflects the relative SHG efficiency for laser excitation parallel versus perpendicular to the main axis of fibril bundles. However, measurement of this parameter is not a simple task due to the many processes involved in tissue response, mostly linear propagation effects, such as birefringence [2,6,10], diattenuation [6], and polarization scrambling [8]. We have recently proposed a comprehensive phenomenological model to account for all these phenomena in thick anisotropic tissues such as rat-tail tendon [9]. This model was successfully used to monitor variations in fibril distribution in tendons upon mechanical stretching [14], and to quantitatively assess fibril organization in human and rat corneas [15].

Nevertheless, while this phenomenological approach proved to be robust and to account for all observed artifactual processes, it had three main limitations. First, it was deduced for scalar fields and therefore theoretically applied only to low-numerical-aperture objectives, whereas SHG microscopy usually relies on strongly focused beams exhibiting polarization mixing and a Gouy phase shift at focus. Second, this phenomenological approach considered uniform fields within the focal volume. In particular, the phase shift between ordinary and extraordinary waves due to birefringence was taken as constant all over the focal volume, although it is expected to continuously vary within its depth. Third, it did not consider optical dispersion in the tissue, which may affect the buildup of SHG signals.

In this paper, we describe numerical simulations of PSHG by a strongly focused beam in anisotropic thick tissues in order to improve the understanding of PSHG microscopy in collagen-rich tissues and to develop reliable methods to extract quantitative parameters from PSHG images. While numerical studies of multiphoton imaging have been reported in the case of isotropic tissues [20–25], the case of anisotropic media has never been addressed so far to the best of our knowledge, due to the complexity introduced by optical anisotropy. In this paper, we addressed the case of high numerical aperture (NA) of 0.95 using a vectorial approach and mapping the variation of optical parameters within the focal volume. We considered a birefringent medium with index dispersion, but without any scattering. Diattenuation and polarization cross-talk, which

*ivan.gusachenko@polytechnique.edu
†marie-claire.schanne-klein@polytechnique.edu

are mainly due to scattering, are therefore not accounted for in these simulations and should be treated using appropriate statistical methods [26,27].

The paper is organized as follows. The next section introduces the theoretical formalism of PSHG and the phenomenological model we developed to account for various artifacts [9], which context is necessary for the discussion of the results presented in this paper. It also presents the general scheme of PSHG calculation in a birefringent tissue with strong focusing. The third section is devoted to the theoretical derivation and the numerical simulation of the incident focal field distribution in the tendon. The same organization is used in the fourth section for nonlinear radiation in the tendon. Finally, the phenomenological approach is reconsidered in the discussion, before we conclude.

II. THEORETICAL BACKGROUND OF PSHG MICROSCOPY IN COLLAGEN TISSUES

A. Nonlinear-optical tensorial response of collagen

We consider a rat-tail tendon fascicle as a model tissue to develop our numerical calculations, which could then be generalized to other collagen-rich tissue. We assume that this rat-tail fascicle is a homogeneous material with uniform linear and nonlinear optical responses. This assumption is valid in this tissue because it is composed of closely packed collagen fibrils that dominate the optical response of the material. This approach, however, does not take into account scattering along the fibrils within the fascicle, which is the main limitation of this work, as mentioned in the Introduction. The collagen fibrils are aligned along a main axis x, which therefore acts as both linear- and nonlinear-optical anisotropy axis. The tissue lies in the focal plane xy of the multiphoton microscope. This rat-tail tendon fascicle is just called the tendon in the following.

The PSHG response is described by its second-order nonlinear susceptibility tensor $\chi^{(2)}_{ijk}$, which links the induced nonlinear polarization $\mathbf{P}^{2\omega}$ to the excitation field $\mathbf{E}^{\omega}$ [28]:

$$P_i^{2\omega} = \chi^{(2)}_{ijk} E_j^{\omega} E_k^{\omega}. \tag{1}$$

Considering that collagen unidimensional tissues like tendon possess cylindrical symmetry [1,2] and assuming Kleinman symmetry, there are only two independent tensor components: $\chi^{(2)}_{xxx}$ and $\chi^{(2)}_{xyy} = \chi^{(2)}_{yxy} = \chi^{(2)}_{yyx} = \chi^{(2)}_{xzz} = \chi^{(2)}_{zxz} = \chi^{(2)}_{zzx}$. The induced nonlinear polarization then reads

$$\begin{aligned} P_x^{(2\omega)} &= \chi^{(2)}_{xxx} E_x^2 + \chi^{(2)}_{xyy} E_y^2 + \chi^{(2)}_{xyy} E_z^2, \\ P_y^{(2\omega)} &= 2\chi^{(2)}_{xyy} E_x E_y, \\ P_z^{(2\omega)} &= 2\chi^{(2)}_{xyy} E_x E_z. \end{aligned} \tag{2}$$

We introduce the ratiometric parameter $\rho = \chi^{(2)}_{xxx}/\chi^{(2)}_{xyy}$ which is sufficient to characterize the PSHG response of the tissue up to a constant intensity factor. For a linearly polarized light at an angle α to the fascicle axis and neglecting the axial components E_z of the electric field, one obtain the widely used equations

$$P_x^{2\omega} \propto \rho \cos^2\alpha + \sin^2\alpha, \quad P_y^{2\omega} \propto \sin 2\alpha. \tag{3}$$

Note that more advanced PSHG approaches consider the full $\chi^{(2)}$ tensor without any assumption about the material symmetry [11]. Such an approach has been successfully applied to thin collagen coatings to get information about the orientational distribution of collagen molecules [11]. Nevertheless, it does not take into account propagation and focalization within the material and is therefore not suitable for thick collagen-rich tissues such as those considered in this work.

B. Phenomenological model of PSHG in tendon

Tendon PSHG imaging has been shown to exhibit several artifacts due to linear propagation effects. Laser excitation is indeed affected by diattenuation and birefringence when propagating within this thick anisotropic tissue, while SHG radiation undergoes polarization scrambling. Tendon birefringence results in a phase shift $\Delta\phi = 2\pi z(n_e - n_o)/\lambda$ that accumulates with depth z between the x- and y-polarized components of the excitation fields [2,9,10]. These fields indeed propagate with different phase velocities c/n_e and c/n_o, where n_e and n_o stand for the extraordinary and ordinary optical indices, respectively. Diattenuation corresponds to the difference $1/\Delta l_a = 1/l_{\alpha=0} - 1/l_{\alpha=\pi/2}$ of inverse attenuation lengths for the incident polarization components parallel ($\alpha = 0$) and perpendicular ($\alpha = \pi/2$) to the tendon fascicle axis [6,9]. It is mostly due to different scattering efficiency depending on whether the incident electric field is parallel or perpendicular to the collagen fibrils. Finally, polarization scrambling corresponds to stochastic polarization rotation due to scattering on misaligned fibrils. It mainly affects SHG data in the case of polarization-resolved detection, as the SH generated with y polarization contributes to the SHG signal detected on the x-polarized channel with the weight η. Otherwise, all polarization components contribute equally to the SHG signal and $\eta = 1$.

These effects have been taken into account in a phenomenological model [9], summarized in the following equation:

$$\begin{aligned} &I^{2\omega}(\alpha,z) \\ &\quad \propto \left(|\rho e^{-z/\Delta l_a}\cos^2\alpha\, e^{i\Delta\phi} + \sin^2\alpha|^2 + \eta e^{-z/\Delta l_a}|\sin 2\alpha|^2\right). \end{aligned} \tag{4}$$

This equation can be reduced to $A\cos 4\alpha + B\cos 2\alpha + C$ to fit the experimental data and to extract the ρ parameter. We also introduce a Δ parameter that is also obtained from the fitting parameters and that unites the relative contributions of y polarization (η) and oscillations due to birefringence (see the detailed derivation in [9]):

$$\Delta = \eta - \frac{\rho}{2}(1 - \cos\Delta\phi). \tag{5}$$

It proved robust for extracting reproducible linear [birefringence $(n_e - n_o)$ and diattenuation Δl_a] and nonlinear (SHG anisotropy ρ) tendon parameters from experimental images acquired at increasing depth and for various incident polarization angles α. Most notably, it enabled the observation of a decrease in ρ due to increasing alignment of fibrils within the focal volume when stretching the tendon in a physiological range [14].

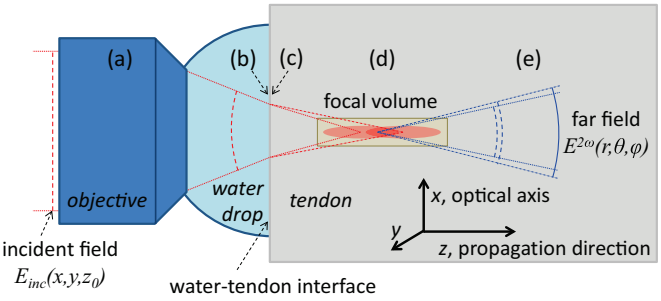

FIG. 1. (Color online) Scheme of PSHG calculation in a tendon. (a) Plane incident wave is mapped onto a converging spherical wave by a model objective lens. (b) Field distribution just before the water-tendon interface is calculated using the angular spectrum method [29]. (c) Field beyond the interface is obtained using appropriate boundary conditions based on [30]. (d) Focal field in the birefringent medium (tendon) is calculated using the model described in [30]. (e) Radiation in the birefringent medium is calculated based on [31,32].

C. Scheme of theoretical approach

In this paper, we develop a theoretical model and perform numerical simulations to overcome the limitations of the previous phenomenological model. We use a vectorial description of the electric fields to account for polarization mixing due to strong focusing and we calculate the electric field distribution all around the focal volume to account for phase variations within this region. The general scheme of calculation is displayed in Fig. 1. (a) The starting point of the calculation is the incident field distribution on the back pupil of the objective. The objective transforms the incident plane wave into a converging spherical wave. (b) For a fixed position of the objective lens $z_{\rm obj}$, we simulate propagation from the objective to the interface between water and tendon by the angular spectrum representation method [29]. (c) According to [30], boundary conditions are used to obtain the field in the tendon near the surface. (d) The focal field distribution is then calculated by a method similar to that of [29] which uses different field propagators for ordinary and extraordinary waves [30]. The obtained field distribution near the focal volume is used to calculate the induced nonlinear polarization of the medium. (e) Finally, radiation of the SHG signal in the birefringent medium is calculated using the Clemmow scaling method [31,32]. This whole procedure is performed at increasing depth within the sample and for different polarization angles α of the incident field to the tendon axis, to obtain $I_{\alpha,z}$ maps. These maps are then processed using Eq. (4), that is, in the same way as experimental data, to discuss the relevance of the phenomenological approach.

All these calculations are performed for different sets of tendon optical parameters. The first parameter is the tendon ordinary index. We use $n_0 = 1.33$, which corresponds to perfect index matching with the immersion medium (water), and $n_0 = 1.5$, which has been reported for tendons [33]. In the latter case, due to index mismatch at the tendon surface, the effective focusing depth $z_{\rm sample}$ within the tendon is different from the coordinate $z_{\rm obj}$ of the objective; $z_{\rm sample} = z_{\rm obj}\, n_{\rm sample}/n_{\rm water}$ in paraxial approximation. For the sake of simplicity, we will always refer to $z_{\rm obj}$. $z_{\rm obj} = 0$ corresponds to a beam focused at the water-tendon interface. The second parameter is the tendon birefringence, for which values $\Delta n = 0$ and $\Delta = 0.007$ are used. While $\Delta n = 0.007$ corresponds to the values experimentally measured in tendon [9,14,33], the value $\Delta n = 0$ was chosen to comparatively assess the effect of birefringence on the determination of other optical parameters. The last parameter is the medium dispersion $d = n_{2\omega} - n_{\omega}$, which affects the phase matching of waves at ω (incident wave) and 2ω (SH wave) during SHG radiation. In our simulations we use $d = 0$ and $d = 0.05 n_o$ (5% dispersion). The 5% value corresponds to values reported in the literature [34], while $d = 0$ was used as a control. Finally, the SHG anisotropy parameter ρ was fixed to 1.36, which was obtained from our experimental data using the phenomenological approach [9]. The simulations were thus performed for a total of eight sets of parameters, as shown in Table I.

TABLE I. Parameter sets used for simulation of SHG radiation intensity. The set no. 8 presumably reproduces actual tendon optical parameters.

Set	1	2	3	4	5	6	7	8
n	1.33	1.33	1.5	1.5	1.33	1.33	1.5	1.5
d (%)	0	5	0	5	0	5	0	5
Δn	0	0	0	0	0.007	0.007	0.007	0.007

III. FOCAL FIELD CALCULATION IN BIREFRINGENT MEDIA

A. Field propagation in a uniform medium

The field distribution of the beam focused by an objective can be obtained using the angular spectrum representation method (see Chap. 3 of [29]). Briefly, the field $\mathbf{E}$ near the beam focus can be expressed through the far field $\mathbf{E}_\infty$ at a reference sphere of radius f (objective focal length) centered at the focus $z = 0$:

$$\mathbf{E}(x,y,z) = \frac{ire^{-ikr}}{2\pi} \iint_{(k_x^2+k_y^2)\leqslant k^2} \mathbf{E}_\infty(k_x,k_y) e^{i[k_x x + k_y y + k_z z]} \frac{1}{k_z} dk_x\, dk_y. \tag{6}$$

Here, $k_z = \sqrt{k^2 - k_x^2 - k_y^2}$ is the longitudinal component of the wave vector, and $r = \sqrt{x^2+y^2+z^2}$. The integral is calculated over a disk of radius k, since we neglect evanescent waves with imaginary k_z. Moreover, the solid angle of illumination is limited by the numerical aperture ($\mathcal{A}$) of the lens, so that we replace k by $k_{\rm max} = k\frac{\mathcal{A}}{n}$.

The far field $\mathbf{E}_\infty$ is obtained from the incident field $\mathbf{E}_{\rm inc}$ using a model lens, which transforms a plane wave into a spherical wave converging to $z = 0$, which is the focal point:

$$\mathbf{E}_\infty = \{t^s[\mathbf{E}_{\rm inc}\cdot\mathbf{n}_\varphi]\mathbf{n}_\varphi + t^p[\mathbf{E}_{\rm inc}\cdot\mathbf{n}_\rho]\mathbf{n}_\theta\}\sqrt{\frac{n_1}{n_2}}\cos\theta. \tag{7}$$

Here, the $\mathbf{n}_\varphi$ and $\mathbf{n}_\rho$ projections of the incident field in the cylindrical coordinate system are mapped onto the $\mathbf{n}_\varphi$ and $\mathbf{n}_\theta$ components in a spherical system for the converging wave. The factor $\sqrt{\frac{n_1}{n_2}}\cos\theta$ ensures energy flux conservation. t^s and

t^p are Fresnel coefficients, which are set to 1 for an optically cleared lens. We suppose that the incident beam is a Gaussian beam collimated on the back pupil of the objective, and has a waist of $w_0 = f$ (considering a slightly overfilled aperture). The beam is linearly polarized in the xy plane with angle α to the x axis. After expressing θ and φ via k_x and k_y, one can calculate $\mathbf{E}$ by introducing Eq. (7) into Eq. (6).

B. Field focusing in a birefringent medium

After propagation from the objective through the immersion medium, the beam strikes the interface with the tendon and further propagates through it. We model the tendon as a birefringent medium, so there will be an ordinary and an extraordinary wave propagating through the tissue. To model the light propagation in the birefringent medium we adapt the formalism proposed by Hacyan and Jáuregui [30].

The Maxwell equations in the absence of free charges and currents are

$$\begin{aligned} \nabla\cdot\mathbf{B} &= 0, \qquad \nabla\times\mathbf{E} + \frac{\partial\mathbf{B}}{\partial t} = 0,\\ \nabla\cdot\mathbf{D} &= 0, \qquad \nabla\times\mathbf{H} - \frac{\partial\mathbf{D}}{\partial t} = 0, \end{aligned} \tag{8}$$

where $\mathbf{D} = \hat{\epsilon}\cdot\mathbf{E}$ and $\mathbf{B} = \mu\mathbf{H}$. For a birefringent medium with the optical axis along Ox, the linear susceptibility is written

$$\hat{\epsilon} = \begin{pmatrix} \epsilon_e & 0 & 0\\ 0 & \epsilon_o & 0\\ 0 & 0 & \epsilon_o \end{pmatrix}, \tag{9}$$

where ϵ_e and ϵ_o are the permittivities parallel and perpendicular to the axis, respectively. One can show that solutions for the Maxwell equations (8) for ordinary and extraordinary monochromatic waves are

$$\begin{aligned} \mathbf{E}^o &= -i\omega\mathbf{e}_x\times\nabla\psi^o,\\ \mathbf{E}^e &= -\frac{1}{\epsilon_o}\nabla\left(\mathbf{e}_x\cdot\nabla\psi^e\right) - \mu\omega^2\psi^e\mathbf{e}_x. \end{aligned} \tag{10}$$

Here, $\mathbf{e}_x$ is a unit vector along Ox, and ψ^o and ψ^e are Hertz potentials satisfying the two equations

$$\begin{aligned} \epsilon_o\mu\omega^2\psi^o + \nabla^2\psi^o &= 0,\\ \epsilon_o\epsilon_e\mu\omega^2\psi^e + \nabla\cdot\hat{\epsilon}\cdot\nabla\psi^e &= 0. \end{aligned} \tag{11}$$

The general solutions of Eq. (11) for $z > 0$ are

$$\begin{aligned} &\psi^{(o,\,e)}(x,y,z)\\ &\quad= \frac{1}{2\pi}\iint dk_x dk_y e^{ik_x x + ik_y y + ik_z^{(o,e)} z}\widetilde{\psi}^{(o,e)}\left(k_x,k_y;z\right), \end{aligned} \tag{12}$$

where $\widetilde{\psi}^{(o,e)}\left(k_x,k_y\right)$ is the Fourier transform of $\psi^{(o,e)}(x,y,z=0)$, and $k_z^{(o,e)}$ in the expression above are solutions to the following equations:

$$\begin{aligned} \epsilon_o\mu\omega^2 - \mathbf{k}^o\cdot\mathbf{k}^o &= 0,\\ \epsilon_o\epsilon_e\mu\omega^2 - \mathbf{k}^e\cdot\hat{\epsilon}\cdot\mathbf{k}^e &= 0. \end{aligned} \tag{13}$$

One can rewrite Eq. (10) as follows:

$$\begin{aligned} \widetilde{\mathbf{E}}^o &= \omega\mathbf{e}_x\times\mathbf{k}^o\widetilde{\psi}^o(\mathbf{k}^o),\\ \widetilde{\mathbf{E}}^e &= \left[\frac{1}{\epsilon_o}(\mathbf{e}_x\cdot\mathbf{k}^e)\mathbf{k}^e - \mu\omega^2\mathbf{e}_x\right]\widetilde{\psi}^e(\mathbf{k}^e). \end{aligned} \tag{14}$$

The focal fields $\mathbf{E}^o$ and $\mathbf{E}^e$ are obtained from $\widetilde{\psi}^{(o,e)}(k_x,k_y;z)$ using Eq. (14) and a subsequent Fourier transform. The total field $\mathbf{E}$ in the medium is

$$\begin{aligned} \mathbf{E} &= \mathbf{E}^o + \mathbf{E}^e\\ &= \left(E_x^e; E_y^o + E_y^e; E_z^o + E_z^e\right) = \left(E_x; E_y; E_z\right). \end{aligned} \tag{15}$$

By definition, there is no ordinary wave component E_x^o along the optical axis. Equation (15) means that in the case of tight focusing discussed in this paper, a wave with any polarization incident on a high-NA objective will produce all five components from Eq. (15), both ordinary and extraordinary ones, and along the x, y, and z axes.

Due to the linearity of the Maxwell equations, we can choose a basis of two incident fields $\mathbf{E}_{\mathrm{inc},1,2}$ and calculate $\mathbf{E}_{1,2}$, which can be used to reproduce the focal field from any incident polarization. To simplify the calculations, we choose

$$\mathbf{E}_{\mathrm{inc},1} = \mathbf{E}_{\mathrm{inc},\parallel} = E_0\mathbf{e}_x, \tag{16}$$

$$\mathbf{E}_{\mathrm{inc},2} = \mathbf{E}_{\mathrm{inc},\perp} = E_0\mathbf{e}_y, \tag{17}$$

and we will use $E_{i\parallel,\perp}$ to denote field components produced by $\mathbf{E}_{\mathrm{inc},\parallel,\perp}$. It should be emphasized that all these field components, except for $E_{x\parallel}$, have both ordinary and extraordinary contributions, as seen from the Eq. (15). Notably, for an incident field polarized at angle α to the x axis, the focal field is written

$$\begin{aligned} \mathbf{E}_\alpha = (&E_{x\parallel}\cos\alpha + E_{x\perp}\sin\alpha, \quad E_{y\parallel}\cos\alpha + E_{y\perp}\sin\alpha,\\ &E_{z\parallel}\cos\alpha + E_{z\perp}\sin\alpha), \end{aligned} \tag{18}$$

where

$$\begin{aligned} E_{x\parallel,\perp} &= E^e_{x\parallel,\perp},\\ E_{y\parallel,\perp} &= E^o_{y\parallel,\perp} + E^e_{y\parallel,\perp},\\ E_{z\parallel,\perp} &= E^o_{z\parallel,\perp} + E^e_{z\parallel,\perp}. \end{aligned} \tag{19}$$

We must then calculate ten field distributions. However, it is expected that $E^o_{y\perp}$ and $E^e_{x\parallel}$ are much larger than all other components, so the fields produced by $\mathbf{E}_{\mathrm{inc},\parallel}$ and $\mathbf{E}_{\mathrm{inc},\perp}$ are "mostly" ordinary and extraordinary, respectively.

C. Boundary conditions between isotropic and birefringent media

As shown in Eq. (12), the calculation of $\psi^{o,e}(x,y,z)$ and therefore of $\mathbf{E}^{o,e}$ requires the values of $\psi^{o,e}(x,y,z=0)$ near the interface between the birefringent medium (tendon) and the isotropic medium (immersion, water). These values are obtained from the incident field using appropriate boundary conditions between the two media. From the work of Hacyan and Jáuregui [30], we deduce boundary conditions for ordinary and extraordinary Hertz potentials. For an interface between a uniform medium (water, permittivity $\epsilon_1 = n^2_{\mathrm{water}}$) and a

birefringent medium (tendon) with permittivity tensor defined in Eq. (9) one obtains

$$\widetilde{\psi}^o = 2\frac{[\mathbf{e}_z \times (\mathbf{Q}+\mathbf{S})]\cdot\widetilde{\mathbf{E}}_{\rm inc}}{(\mathbf{Q}+\mathbf{S})\cdot[(\mathbf{P}+\mathbf{R})\times\mathbf{e}_z]},$$
$$\widetilde{\psi}^e = -2\frac{[\mathbf{e}_z \times (\mathbf{P}+\mathbf{R})]\cdot\widetilde{\mathbf{E}}_{\rm inc}}{(\mathbf{Q}+\mathbf{S})\cdot[(\mathbf{P}+\mathbf{R})\times\mathbf{e}_z]}, \tag{20}$$

where $\widetilde{\mathbf{E}}_{\rm inc}$ is the Fourier transform of the incident field near the tendon surface, and

$$\mathbf{P} = -\omega k_z^o \mathbf{e}_y, \quad \mathbf{Q} = \epsilon_o^{-1} k_x \mathbf{k}_\perp - \mu\omega^2 \mathbf{e}_x,$$
$$\mathbf{R} = \frac{\omega k_x}{\mu k_z}[\mathbf{e_z}\times\mathbf{k}_\perp] - \frac{\epsilon_o\omega^3}{k_z}\mathbf{e}_y + \frac{\epsilon_o k_y}{\epsilon_1 k_z}\mathbf{k}_\perp, \tag{21}$$
$$\mathbf{S} = -\frac{\omega^2}{k_z}k_z^e\mathbf{e}_x + \frac{k_x k_z^e}{\epsilon_1 k_z}\mathbf{k}_\perp.$$

In the equations above, k_z simply denotes the longitudinal component of the wave vector in the isotropic medium (water); $\mathbf{k}_\perp = (k_x, k_y, 0)$ is the component transverse to the beam propagation, which does not change on the tendon-water interface due to the boundary conditions.

The implementation of these numerical calculations, for both the fields outside and inside the tendon, are performed in MATLAB using chirp Z transform according to [35]. This technique provides significant increase in calculation speed compared to both direct calculation of Eq. (6) and fast Fourier transform with zero padding [35]. To additionally increase the speed, the calculations were performed on a graphics processing unit (GPU) using the Acceleryes Jacket plug-in for MATLAB. The typical time required for all the field components for a $64 \times 64 \times 256$ array was on the order of a few seconds.

D. Results and discussion

1. Intensity distribution

The calculated beam intensity distribution for two tendon indices ($n_o = 1.33$ and $n_o = 1.5$) and for two incident linear polarizations (parallel and perpendicular to the tendon axis) is displayed in Fig. 2. As explained previously, we use the notations $E_{i,\parallel,\perp}$ for focal field components resulting from the incident field $E_{\mathrm{inc},\parallel,\perp}$. Intensities are calculated for the objective position $z_{\rm obj} = 50\ \mu$m. The birefringence is set to $\Delta n = n_e - n_o = 0.007$, as reported for tendons in [9,33]. Within each of two sets with different n_o, the intensities are normalized to the maximal intensity of the field $E_{x\perp}$. The intensities for $n_o = 1.33$ are larger than those for $n_o = 1.5$ by a factor of 1.441. Indeed, the effective focal volume is wider for $n_o = 1.5$ due to spherical aberrations. As in both cases the total beam energy flux is the same, the wider focal volume for $n_o = 1.5$ leads to a smaller intensity.

The largest components produced by $E_{\mathrm{inc},\parallel}$ and $E_{\mathrm{inc},\perp}$ are $E_{x\parallel}$ and $E_{y\perp}$, as expected [Figs. 2(a), 2(d), and 2(h), 2(k)]. The intensity of z-polarized fields attains up to 9% [Fig. 2(l)] of that of the main components, while the intensities of $E_{y\parallel}$ and $E_{x\perp}$ do not exceed 1% [Fig. 2(e)]. Due to the high numerical aperture, the wave created by $E_{\mathrm{inc},\parallel}$ ($E_{\mathrm{inc},\perp}$) is not purely extraordinary (ordinary), but has a small contribution of its orthogonal counterpart. However, for simplicity, we will refer to the field produced by $E_{\mathrm{inc},\parallel}$ (incident field parallel to the tendon axis) as the extraordinary component, and to that produced by $E_{\mathrm{inc},\perp}$ (incident field perpendicular to the tendon axis) as the ordinary component.

The shape of the focal field distribution is less regular for $n_o = 1.5$ than for $n_o = 1.33$ due to spherical aberrations originating from the index mismatch on the surface. However, the extraordinary components for $n_e = 1.337$ are also distorted due to an index slightly different from 1.33. For the case of $n_o = 1.5$, the secondary (smaller) components are axially displaced with respect to the main components due to index mismatch.

2. Phase distribution and birefringence

As can be seen from Fig. 2, the effect of birefringence on the focal field intensity is limited. In contrast, the birefringence affects the relative phase of the ordinary and extraordinary components of the beam, as they propagate with different indices n_o and n_e. This phase shift due to birefringence is observed in the x component of the nonlinear polarization [see Eq. (3)] because it mixes contributions obtained from the ordinary (proportional to E_y^2) and extraordinary (proportional to E_x^2) incident fields [9]. When the phase difference of these contributions is π, the two terms interfere destructively.

In this simulation, we take into account only the largest components $E_{x\parallel}$ and $E_{y\perp}$ to calculate the phase shift within the focal volume. It is then obtained as the complex phase of the product $\arg[(E_{x\parallel}^2)^\dagger E_{y\perp}^2]$. The average phase across the focal volume is weighted by the overlap of the two components which is calculated as $|E_{x\parallel}|^2|E_{y\perp}|^2$. The phase is averaged over a zone $\mathcal{S}$ which encompasses 90% of the overlap. More precisely, the average phase at a certain depth is calculated in the following way:

$$\overline{\Delta\phi} = \frac{\iiint_{\mathcal{S}} \arg\left[\left(E_{x\parallel}^2\right)^\dagger E_{y\perp}^2\right]|E_{x\parallel}|^2|E_{y\perp}|^2 d^3\mathbf{r}}{\iiint_{\mathcal{S}} |E_{x\parallel}|^2|E_{y\perp}|^2 d^3\mathbf{r}}. \tag{22}$$

The phase shift between $(E_{x\parallel})^2$ and $(E_{y\perp})^2$ within the focal volume is shown in Figs. 3(a)–3(d). In each subfigure (a)–(d), the inner region corresponds to the phase variation within the zone $\mathcal{S}$ with respect to the average phase $\overline{\Delta\phi}$ over this zone, which is given at the bottom. The phase shift in the head of the beam is larger than that in its tail. One can see from the scale bars that the phase dispersion across $\mathcal{S}$ is roughly twice larger at 50 μm than at 25 μm. However, it is approximately of the same extent for $n_o = 1.33$ and for $n_o = 1.5$.

The phase difference averaged across the focal volume as a function of focusing depth is shown in Fig. 3(e). The phase shift π, which corresponds to destructive interference, occurs near ~27–30 μm, in agreement with our previous experimental measurements [9]. Notably, the phase difference accumulated with depth between extraordinary and ordinary polarization depends on the index of the medium. Indeed, in the paraxial approximation the phase shift between squared fields at a fixed $z_{\rm sample}$ can be written as

$$\Delta\phi = 2\frac{2\pi}{\lambda}\Delta n\, z_{\rm sample} = \frac{4\pi}{\lambda}\Delta n\, z_{\rm obj}\frac{n_{\rm sample}}{n_{\rm water}}. \tag{23}$$

It is proportional to both the medium index and birefringence. Fitting the data in Fig. 3(e) with this equation, one gets $\Delta n \approx$

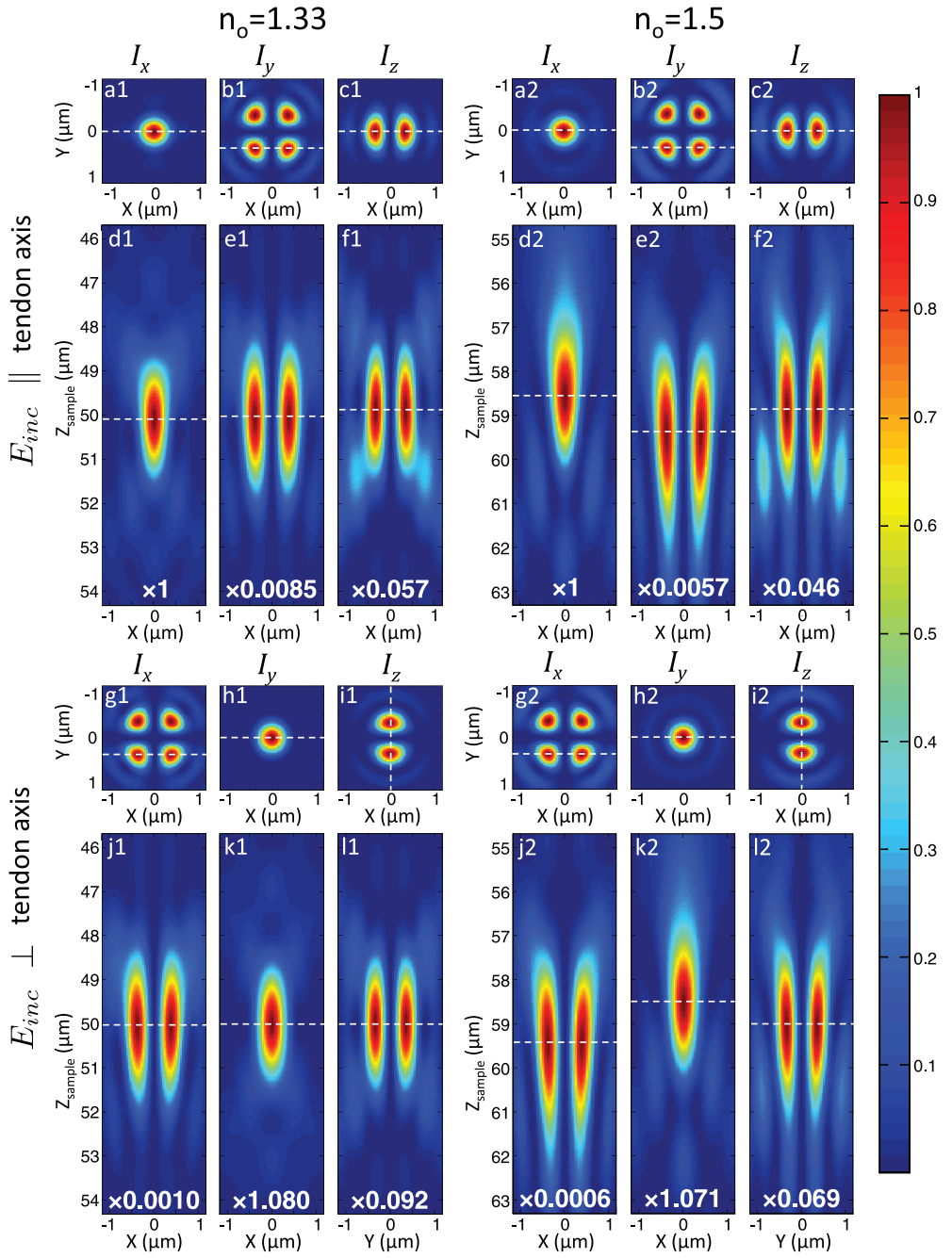

FIG. 2. (Color online) Intensity distribution of the simulated focal field for an objective with NA of 0.95 in a birefringent medium normalized to the x component of the x-polarized incident field $I_{x\|}$ (a),(d). The objective z coordinate is $z_{\text{obj}} = 50$ μm. (a),(d),(g),(j) x-polarized component; (b),(e),(h),(k) y-polarized component; (c),(f),(i),(l) z-polarized component. Calculations for (a1)–(l1) $n_o = 1.33$; (a2)–(l2) $n_o = 1.5$; (a)–(f) incident beam polarized along the tendon optical axis; (g)–(l) incident beam polarized perpendicularly to the tendon axis. Intensity profile (a)–(c),(g)–(i) in the xy plane; (d)–(f),(j)–(k) in the xz plane; (l) in the yz plane. White dotted lines on xy slices indicate the xz slice position, and vice versa. Numbers indicate the intensity factor with respect to the $I_{x\|}$ intensity. Intensities for $n_o = 1.33$ are larger than those for $n_o = 1.5$ by a factor of 1.441. The difference in z position between $n_o = 1.33$ and $n_o = 1.5$ is due to the different index mismatch.

0.0071 for $n_o = 1.33$ and $\Delta n \approx 0.0072$ for $n_o = 1.5$, which is very close to the value 0.007 used for the calculation in spite of the nonparaxial focusing.

The normalized spatial overlap is displayed as a function of focusing depth in Fig. 3(f). One can see that the ordinary and extraordinary components do not separate significantly over the whole simulated range (up to 80 μm depth). Remarkably, the separation is more pronounced for the case $n_o = 1.33$ than for $n_o = 1.5$. This can be understood because in the second case the relative difference in index mismatch between ordinary and extraordinary waves is marginal ($1.507 - 1.33 = 0.177$ versus $1.5 - 1.33 = 0.170$), while it is substantial in the first case (0.007 for the extraordinary wave, while the ordinary wave is index matched).

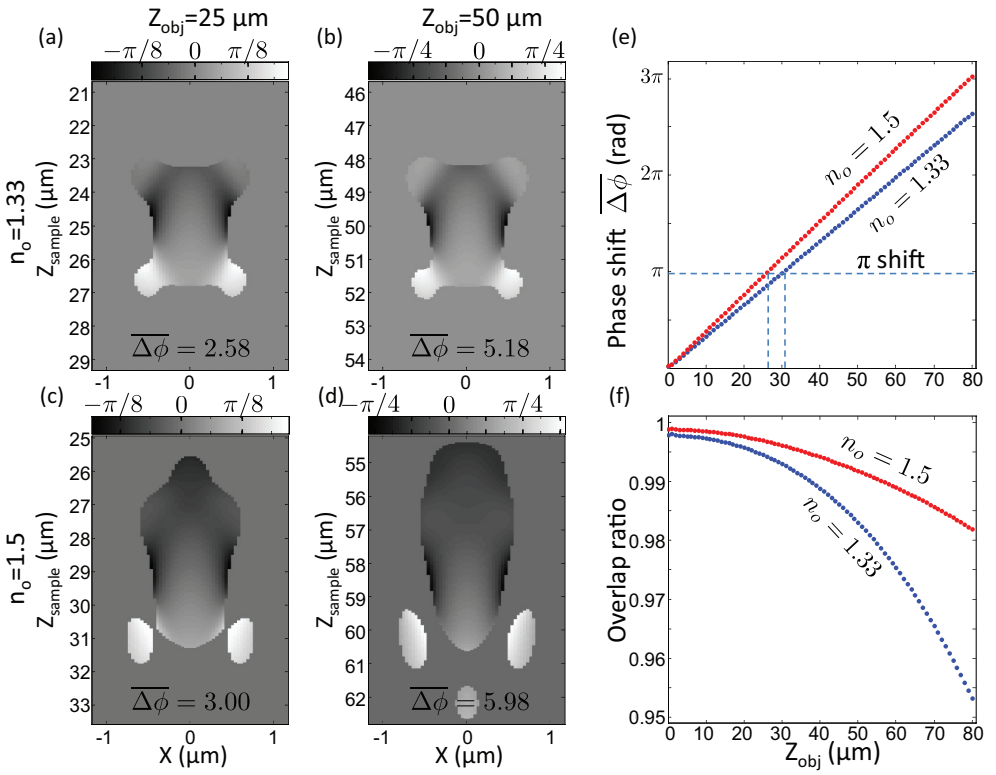

FIG. 3. (Color online) (a)–(d) Simulated phase shift between squared x- and y-polarized fields produced by $E_{\mathrm{inc},x}$ and $E_{\mathrm{inc},y}$, within a zone encompassing 0.9 of the field overlap, with respect to the average phase $\overline{\Delta\phi}$ over this zone. Calculation (a),(b) for $n_o = 1.33$; (c),(d) for $n_o = 1.5$; (a),(c) at 25 μm focusing depth; (b),(d) at $z_{\mathrm{obj}} = 50$ μm focusing depth. (e) Averaged phase shift between $(E_{x\parallel})^2$ and $(E_{y\perp})^2$ and (f) overlap between ordinary and extraordinary components as a function of focusing depth for $n_o = 1.33$ (blue) and $n_o = 1.5$ (red).

3. *Conclusion*

In this section, we calculated the focal field distribution in a birefringent medium for a tightly focused beam and characterized the phase shift between ordinary and extraordinary waves. The phase shift is not uniform within the focal volume, and its average is proportional to the depth of focusing, as expected. The birefringence obtained from the simulated data is in perfect agreement with the value used for calculation, which means that the paraxial approximation can be used for extracting birefringence from the experimental data. Additionally, a slight separation of focal volumes is observed at larger depths. The effect of the birefringence on the focal field intensity distribution is minimal and is due to the additional spherical aberrations it creates.

IV. SH RADIATION IN TENDON

A. Radiation of a punctual dipole in a birefringent medium

The focal field calculated in the previous section is used to calculate the induced polarization at double frequency using Eq. (2). While the induced polarization is easily calculated, the analytical calculation of radiation produced by this polarization density in a birefringent medium is not a trivial task. The mathematical formulation of the radiation problem consists in the following. In order to find the radiated intensity one has to derive a particular far-field solution of the Maxwell equations

$$\nabla \times \mathbf{E} = -\frac{\partial \mathbf{B}}{\partial t}, \qquad \nabla \times \mathbf{H} = \mathbf{J}_S + \frac{\partial \mathbf{D}}{\partial t} \tag{24}$$

in the medium with the following constitutive equations:

$$\mathbf{D} = \varepsilon_0 \mathbf{E} + \mathbf{P} = \begin{pmatrix} \epsilon_e & 0 & 0 \\ 0 & \epsilon_o & 0 \\ 0 & 0 & \epsilon_o \end{pmatrix} \mathbf{E}, \quad \mathbf{B} = \mu \mathbf{H}. \tag{25}$$

$\epsilon_e = n_e^2$ and $\epsilon_o = n_o^2$ are the dielectric permittivities along and perpendicular to the axis of symmetry, as introduced in Sec. III B. In the equations above, $\mathbf{J}_S = \frac{\partial \mathbf{P}^{(2\omega)}}{\partial t}$ is the source current, produced by the induced polarization $\mathbf{P}^{(2\omega)}$.

The solution of these equations is obtained from the fundamental solution, that is, the field $\mathbf{E}^j(\mathbf{r})$ radiated by a punctual dipole $\mathbf{p}^j = \mathbf{e}_j \delta(\mathbf{r})$ along the j axis, as

$$\mathcal{E}_i^j = \iiint E_i^j(\mathbf{r} - \mathbf{r}') P_j^{(2\omega)}(\mathbf{r}') d\mathbf{r}'. \tag{26}$$

For an isotropic medium, the fundamental solution is known to be a spherical wave of the form e^{ikr}/kr.

In a uniaxial medium, a radiating dipole can be split into two components (parallel and perpendicular to the optical axis) for which the radiation is expected to be different due to anisotropy. An elegant solution for dipole radiation in a uniaxial medium was proposed by Clemmow [31,32]. The method relies on known solutions for the field in vacuum and

is based on different scaling of these solutions in a birefringent medium for ordinary and extraordinary waves.

Below, we present the electromagnetic field radiated by x-, y-, and z-oriented dipoles as given in [31]. Additionally, the expressions are simplified by applying the far-field approximation. All fields are written down in the spherical coordinate system associated with the axis of beam propagation (and SHG detection) z. For a dipole oriented along the tendon axis x, its radiation is purely an extraordinary wave. However, the radiation of a dipole perpendicular to the tendon axis is neither purely ordinary nor purely extraordinary, but is a mixture of the two. It was shown by Clemmow [32] that such a punctual dipole can be split into two components, so that each one generates exclusively either an ordinary or an extraordinary wave. In the following, the electric field is given in units of $\frac{k^2}{4\pi\varepsilon_{0c}} n_o$, so this factor is omitted in the expressions. We also introduce the effective radius vectors for ordinary ($\sqrt{\epsilon_o}\mathbf{r}$) and extraordinary ($\mathbf{R}$) waves, and their lengths $\sqrt{\epsilon_o} r$ and R, respectively.

$$\mathbf{R} = (\sqrt{\epsilon_e}x, \sqrt{\epsilon_o}y, \sqrt{\epsilon_o}z), \quad R = \sqrt{\epsilon_e x^2 + \epsilon_o(y^2+z^2)},$$
$$\sqrt{\epsilon_o}\mathbf{r} = \sqrt{\epsilon_o}(x,y,z), \quad \sqrt{\epsilon_o} r = \sqrt{\epsilon_o}(x^2+y^2+z^2). \tag{27}$$

The radiated field for an x-oriented dipole reads

$$E_\theta^x = i\cos\theta\cos\varphi \frac{\epsilon_e r^2}{R^2}\frac{e^{ikR}}{kR} = T_\theta^{e,x}\frac{e^{ikR}}{kR},$$
$$E_\varphi^x = -i\sin\varphi \frac{\epsilon_e r^2}{R^2}\frac{e^{ikR}}{kR} = T_\varphi^{e,x}\frac{e^{ikR}}{kR}, \tag{28}$$

where θ and φ are the polar and azimuthal angles in the spherical coordinate reference frame associated with the z axis, with the ray $\varphi = 0$ along the x axis [see Fig. 4(a)]. $k = 2\pi/\lambda$ is the wave number in vacuum.

The radiated field for a y-oriented dipole reads

$$E_\theta^y = i\frac{\sin\varphi\cos\theta}{\sin^2\theta\sin^2\varphi+\cos^2\theta}\left(\frac{e^{ik\sqrt{\epsilon_o}r}}{k\sqrt{\epsilon_o}r} - \sin^2\theta\cos^2\varphi\frac{\epsilon_e r^2}{R^2}\frac{e^{ikR}}{kR}\right) = T_\theta^{o,y}\frac{e^{ik\sqrt{\epsilon_o}r}}{k\sqrt{\epsilon_o}r} + T_\theta^{e,y}\frac{e^{ikR}}{kR},$$
$$E_\varphi^y = i\frac{\cos\varphi}{\sin^2\theta\sin^2\varphi+\cos^2\theta}\left(\cos^2\theta\frac{e^{ik\sqrt{\epsilon_o}r}}{k\sqrt{\epsilon_o}r} + \sin^2\theta\sin^2\varphi\frac{\epsilon_e r^2}{R^2}\frac{e^{ikR}}{kR}\right) = T_\varphi^{o,y}\frac{e^{ik\sqrt{\epsilon_o}r}}{k\sqrt{\epsilon_o}r} + T_\varphi^{e,y}\frac{e^{ikR}}{kR}. \tag{29}$$

The radiated field for a z-oriented dipole reads

$$E_\theta^z = -i\frac{\sin\theta}{\sin^2\theta\sin^2\varphi+\cos^2\theta}\left(\sin^2\varphi\frac{e^{ik\sqrt{\epsilon_o}r}}{k\sqrt{\epsilon_o}r} + \cos^2\theta\cos^2\varphi\frac{\epsilon_e r^2}{R^2}\frac{e^{ikR}}{kR}\right) = T_\theta^{o,z}\frac{e^{ik\sqrt{\epsilon_o}r}}{k\sqrt{\epsilon_o}r} + T_\theta^{e,z}\frac{e^{ikR}}{kR},$$
$$E_\varphi^z = -i\frac{\sin\theta\cos\theta\sin\varphi\cos\varphi}{\sin^2\theta\sin^2\varphi+\cos^2\theta}\left(\frac{e^{ik\sqrt{\epsilon_o}r}}{k\sqrt{\epsilon_o}r} - \frac{\epsilon_e r^2}{R^2}\frac{e^{ikR}}{kR}\right) = T_\varphi^{o,z}\frac{e^{ik\sqrt{\epsilon_o}r}}{k\sqrt{\epsilon_o}r} + T_\varphi^{e,z}\frac{e^{ikR}}{kR}. \tag{30}$$

The expressions on the right sides highlight that Eqs. (28)–(30) behave in the same way: $\frac{e^{ik\sqrt{\epsilon_o}r}}{k\sqrt{\epsilon_o}r}$ and $\frac{e^{ikR}}{kR}$ are propagative terms for ordinary and extraordinary waves, respectively, while $T_{\theta,\varphi}^{e,o;x,y,z}$ encompass the angular dependence of the φ and θ components and are specific for extraordinary or ordinary waves generated by x-, y-, and z-oriented dipoles (with $T_{\theta,\varphi}^{o,x} = 0$).

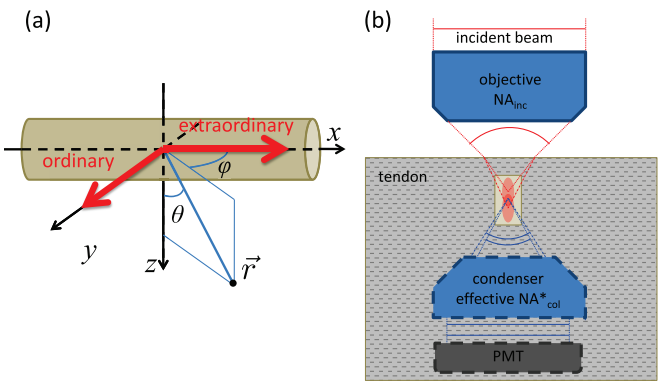

FIG. 4. (Color online) (a) The field inside the tendon is split into ordinary and extraordinary components which experience different refractive indices. (b) In the calculation scheme, the intensity detector is situated within the tendon. The emission diagrams measured by the detector are thus not perturbed by the tendon-water interface.

B. Calculation of the radiation integral

In order to calculate the total fields, one has to integrate these fundamental solutions over the radiating volume as shown in Eq. (26):

$$\mathcal{E}_{\theta,\varphi}^i(\mathbf{r}) = \iiint T_{\theta,\varphi}^{o,i}(\mathbf{r}-\mathbf{r}')P_i^{(2\omega)}(\mathbf{r}')\frac{e^{-ik\sqrt{\epsilon_o}|\mathbf{r}-\mathbf{r}'|}}{k\sqrt{\epsilon_o}\,|\mathbf{r}-\mathbf{r}'|}d^3\mathbf{r}'$$
$$+ \iiint T_{\theta,\varphi}^{e,i}(\mathbf{r}-\mathbf{r}')P_i^{(2\omega)}(\mathbf{r}')\frac{e^{-ik|\mathbf{R}-\mathbf{R}'|}}{k\,|\mathbf{R}-\mathbf{R}'|}d^3\mathbf{r}'. \tag{31}$$

We choose the origin $\mathbf{r} = \mathbf{0}$ somewhere in the radiative volume. The vector $\mathbf{r}$ denotes points in the far-field zone, while $\mathbf{r}'$ denotes points in the excitation volume where the nonlinear polarization is induced, so $r \gg r'$. In this case, $|\mathbf{r}-\mathbf{r}'|$ can be developed in a Taylor series by the powers of $\mathbf{r}'/r$. In the dipole approximation we keep only the first term:

$$|\mathbf{r}-\mathbf{r}'| = \sqrt{(\mathbf{r}-\mathbf{r}')^2} = \sqrt{r^2 - 2\mathbf{r}\cdot\mathbf{r}' + r'^2} \approx r - \mathbf{n}\cdot\mathbf{r}', \tag{32}$$

where $\mathbf{n} = \mathbf{r}/r$. We assume that for a chosen $\mathbf{r}$, all functions of $|\mathbf{r} - \mathbf{r}'|$ are constant across the radiative volume except for rapidly varying exponentials. Introducing Eq. (32) in the integral Eq. (31), we obtain

$$\begin{aligned}\mathcal{E}^{i}_{\theta,\varphi}(r;\theta,\varphi) &= T^{o,i}_{\theta,\varphi}(\theta,\varphi)\frac{e^{ik\sqrt{\epsilon_o}r}}{k\sqrt{\epsilon_o}r}\iiint P^{(2\omega)}_i(\mathbf{r}')e^{-ik\sqrt{\epsilon_o}\mathbf{n}\cdot\mathbf{r}'}d^3\mathbf{r}' \\ &\quad + T^{e,i}_{\theta,\varphi}(\theta,\varphi)\frac{e^{ikR}}{kR}\iiint P^{(2\omega)}_i(\mathbf{r}')e^{-ik\mathbf{N}\cdot\mathbf{R}'}d^3\mathbf{r}' \\ &= \mathcal{E}^{o,i}_{\theta,\varphi}(r;\theta,\varphi) + \mathcal{E}^{e,i}_{\theta,\varphi}(r;\theta,\varphi), \qquad (33)\end{aligned}$$

where $\mathbf{N} = \mathbf{R}/R$. The scalar integrals $\mathcal{P}^i_o(\theta,\varphi) = \iiint P^{(2\omega)}_i(\mathbf{r}')e^{-ik\sqrt{\epsilon_o}\mathbf{n}\cdot\mathbf{r}'}d^3\mathbf{r}'$ and $\mathcal{P}^i_e(\theta,\varphi) = \iiint P^{(2\omega)}_i(\mathbf{r}')e^{-ik\mathbf{N}\cdot\mathbf{R}'}d^3\mathbf{r}'$ reflect the angular efficiency of SH radiation by a given focal distribution of induced polarization $P^{(2\omega)}_i$. Additionally, the angular dependence is shaped by the $T^{o,i}_{\theta,\varphi}$ and $T^{e,i}_{\theta,\varphi}$ terms.

The angular intensity distribution is calculated as the sum of the squared absolute values for the θ and φ projections of the electric field:

$$\begin{aligned}\mathcal{I}(r;\theta,\varphi) &= \left|\mathcal{E}^{o,y}_{\theta} + \mathcal{E}^{o,z}_{\theta} + \mathcal{E}^{e,x}_{\theta} + \mathcal{E}^{e,y}_{\theta} + \mathcal{E}^{e,z}_{\theta}\right|^2 \\ &\quad + \left|\mathcal{E}^{o,y}_{\varphi} + \mathcal{E}^{o,z}_{\varphi} + \mathcal{E}^{e,x}_{\varphi} + \mathcal{E}^{e,y}_{\varphi} + \mathcal{E}^{e,z}_{\varphi}\right|^2. \qquad (34)\end{aligned}$$

One can see from Eq. (33) that the cross terms between ordinary and extraordinary components contain the factor $e^{ik(r\sqrt{\epsilon_o}-R)}$, which oscillates as a function of r. For propagation along the z axis, the extraordinary wave has an effective index close to n_e, so the oscillation period is about $\lambda/(n_e - n_o)$. For a birefringence of 0.007 it gives about 120 μm, which for a 500-μm-thick tendon is equivalent to several periods. It is thus reasonable to consider ordinary and extraordinary waves as mutually incoherent, which allows these cross terms to be neglected.

In a real experimental setup, the radiation diagrams $\mathcal{I}(r;\theta,\varphi)$ in the tendon are altered on the tendon-water interface, which precedes the detectors. Calculating angular diagrams outside the tendon would require the explicit introduction of such an interface between the birefringent and isotropic media. An alternative way is to assume that the SHG signal is detected by a virtual detector situated within the tendon [Fig. 4(b)]. If we neglect the internal reflection, the total intensity in either configuration is the same, but the original diagrams $\mathcal{I}(r;\theta,\varphi)$ are more informative than those changed by the interface, as they reflect the actual phase-matching properties. We adopt the latter configuration [Fig. 4(b)], for which the total radiated intensity for a given angle α of the incident beam polarization and for a given $z_{\rm obj}$ is calculated as follows:

$$I(\alpha, z_{\rm obj}) = r^2\iint \mathcal{I}(r;\theta,\varphi)\big|_{\alpha,z_{\rm obj}}\sin\theta d\theta d\varphi. \qquad (35)$$

As the angular coordinates further need to be discretized for numerical implementation, we will use n_x,n_y instead of (θ,φ) in the following, so that $\mathcal{E}(r;\theta,\varphi) = \mathcal{E}(r;n_x,n_y)$. n_x and n_y are defined as

$$n_x = \sin\theta\cos\varphi, \quad n_y = \sin\theta\sin\varphi. \qquad (36)$$

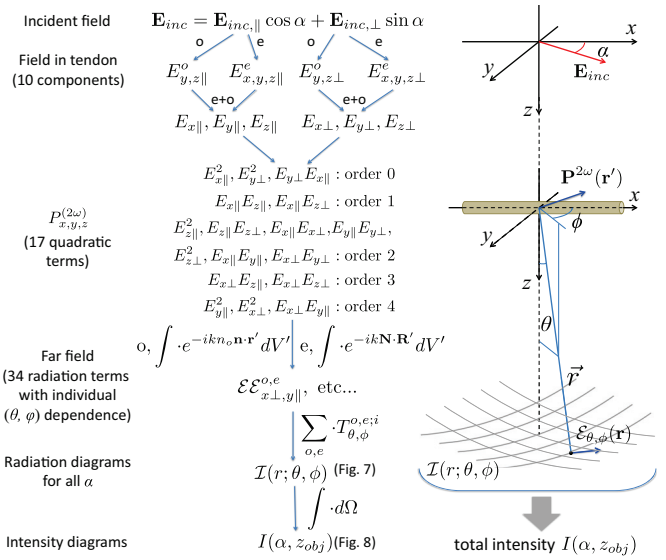

FIG. 5. (Color online) Data flow of PSHG numerical calculation. For two components $E_{\rm inc,\parallel}$ and $E_{\rm inc,\perp}$ of the incident field, ten components $E^{o,e}_{i;\parallel,\perp}$ of the focal field are calculated in the tendon. The induced nonlinear polarization $\mathbf{P}^{2\omega}_i$ then contains 17 quadratic terms of different order and symmetry. Each of these terms produces an ordinary $\mathcal{E}\mathcal{E}^o$ and an extraordinary $\mathcal{E}\mathcal{E}^e$ radiation component (34 total). Radiation diagrams $\mathcal{I}(\theta,\varphi)$ for any chosen α are then calculated using these components $\mathcal{E}\mathcal{E}$ and their respective angular dependences $T^{o,e;i}_{\theta,\varphi}$. Integration of $\mathcal{I}(\theta,\varphi)|_{\alpha,z_{\rm obj}}$ over the solid angle of radiation produces intensity diagrams $I(\alpha,z_{\rm obj})$.

C. Simplification of the calculation using relative order of magnitude and symmetry of the SH radiation components

In Sec. III it was shown that as many as six components are required to reproduce the focal field created by an arbitrary incident polarization: $E_{x\parallel}$, $E_{y\parallel}$, $E_{z\parallel}$, $E_{x\perp}$, $E_{y\perp}$, and $E_{z\perp}$ as defined in Eq. (19) and summarized in Fig. 5. For the induced polarization density it implies

$$\begin{aligned}P^{(2\omega)}_x &\propto \rho(E_{x\parallel}\cos\alpha + E_{x\perp}\sin\alpha)^2 \\ &\quad + (E_{y\parallel}\cos\alpha + E_{y\perp}\sin\alpha)^2 \\ &\quad + (E_{z\parallel}\cos\alpha + E_{z\perp}\sin\alpha)^2, \qquad (37)\end{aligned}$$

$$P^{(2\omega)}_y \propto 2(E_{x\parallel}\cos\alpha + E_{x\perp}\sin\alpha)(E_{y\parallel}\cos\alpha + E_{y\perp}\sin\alpha), \qquad (38)$$

$$P^{(2\omega)}_z \propto 2(E_{x\parallel}\cos\alpha + E_{x\perp}\sin\alpha)(E_{z\parallel}\cos\alpha + E_{z\perp}\sin\alpha). \qquad (39)$$

Instead of numerically calculating $P^{(2\omega)}_i$ and the resulting radiation for every polarization angle α of the incident field, one can calculate the radiation for a finite number of quadratic terms $E_{i,\parallel,\perp}E_{j,\parallel,\perp}$ and use it to instantly obtain the radiation at any given α according to Eqs. (37)–(39). In light of the previous section, one would need to calculate both ordinary and extraordinary integrals $\mathcal{P}^o$ and $\mathcal{P}^e$ for as many as 17 quadratic terms such as $E_{x\parallel}E_{x\parallel}$, $E_{x\parallel}E_{x\perp}$, . . . etc. [nine terms from Eq. (37), four from Eq. (38), and four from Eq. (39);

see Fig. 5). In the following, we will designate these integrals $\mathcal{EE}^{o,e}$, such as, for example [see Eq. (33)],

$$\mathcal{EE}^{o}_{x\parallel,x\perp} = \iiint E_{x\parallel} E_{x\perp} e^{-ik\sqrt{\epsilon_o}\mathbf{n}\cdot\mathbf{r}'} d^3\mathbf{r}', \tag{40}$$

$$\mathcal{EE}^{e}_{y\parallel,z\perp} = \iiint E_{y\parallel} E_{z\perp} e^{-ik\mathbf{N}\cdot\mathbf{R}'} d^3\mathbf{r}'. \tag{41}$$

However, as shown previously (see Fig. 2), the six field components differ significantly in intensity, which allows one to separate the field components into three orders of magnitude:

$$\begin{aligned} &E_{x\parallel}, E_{y\perp}: \text{order 0},\\ &E_{z\parallel}, E_{z\perp}: \text{order 1},\\ &E_{y\parallel}, E_{x\perp}: \text{order 2}, \end{aligned} \tag{42}$$

where order 0 corresponds to the strongest field. When multiplied by one another, they are arranged in five orders as follows:

$$\begin{aligned} E^2_{x\parallel}, E^2_{y\perp}, E_{y\perp}E_{x\parallel}&: \text{order 0},\\ E_{x\parallel}E_{z\parallel}, E_{x\parallel}E_{z\perp}&: \text{order 1},\\ E^2_{z\parallel}, E_{z\parallel}E_{z\perp}, E^2_{z\perp}, E_{x\parallel}E_{x\perp},&\\ E_{y\parallel}E_{y\perp}, E_{x\parallel}E_{y\parallel}, E_{x\perp}E_{y\perp}&: \text{order 2},\\ E_{x\perp}E_{z\parallel}, E_{x\perp}E_{z\perp}&: \text{order 3},\\ E^2_{y\parallel}, E^2_{x\perp}, E_{x\perp}E_{y\parallel}&: \text{order 4}. \end{aligned} \tag{43}$$

We should note that this separation is not strict, and additionally may depend on the numerical aperture of the objective. In practice, this approach allows for estimating contributions from different components. For example, one may compare the scalar field approximation (only the 0 order enabled) with vectorial focusing (all five orders enabled). Also, it is possible to qualitatively assess the contributions of $E_{z\perp,\parallel}$ fields (first order) and smaller $E_{x\perp}$ and $E_{y\parallel}$ fields (second order).

The calculation of the integrals $\mathcal{EE}^{o}$ and $\mathcal{EE}^{e}$ can also be simplified by considering the symmetry of the focal field components. According to our simulations, the focal field components are either symmetric or antisymmetric with respect to x- and y-coordinate inversion, as displayed in the Fig. 6. We denote these symmetry classes with two digits, one for each mirror plane, 0 standing for symmetric and 1 for antisymmetric behavior with respect to axis inversion. For example, the class 01 signifies that the function is

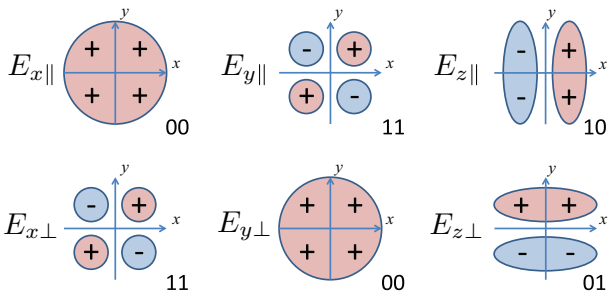

FIG. 6. (Color online) Symmetry of the focal field with respect to the inversion of x and y coordinates. The two largest components $E_{x\parallel}$ and $E_{y\perp}$ are symmetric with respect to both inversions; the smallest components $E_{y\parallel}$ and $E_{x\perp}$ are fully antisymmetric. The E_z components are symmetric with respect to one inversion and antisymmetric with respect to the other.

symmetric with respect to x-coordinate inversion (plane of mirror symmetry $y = 0$), and antisymmetric with respect to y-coordinate inversion (plane of inversion symmetry $x = 0$). The symmetries for the terms written in Eq. (43) can be easily deduced and are shown below:

$$\begin{aligned} E^2_{x\parallel}, E^2_{x\perp}, E^2_{y\parallel}, E^2_{y\perp}, E^2_{z\parallel},&\\ E^2_{z\perp}, E_{y\perp}E_{x\parallel}, E_{x\perp}E_{y\parallel}&: \text{class 00},\\ E_{z\parallel}E_{x\parallel}, E_{z\perp}E_{x\perp}&: \text{class 01},\\ E_{z\parallel}E_{x\perp}, E_{z\perp}E_{x\parallel}&: \text{class 10},\\ E_{z\perp}E_{z\parallel}, E_{x\parallel}E_{x\perp}, E_{x\parallel}E_{y\parallel},&\\ E_{y\perp}E_{y\parallel}, E_{y\perp}E_{x\perp}&: \text{class 11}. \end{aligned} \tag{44}$$

Then it is only necessary to numerically calculate the radiation terms $\mathcal{EE}^{o,e}$ for a single quadrant, for example, $x > 0, y > 0$, as the values in the other quadrants can be deduced according to Eq. (44). A summary of the calculation data flow is depicted in Fig. 5. In order to obtain all necessary components for SH radiation produced at a fixed z_{obj} and at any polarization angle α of the incident field, one must numerically calculate 34 integrals (17 for both ordinary and extraordinary components) in a single quadrant ($x > 0, y > 0$). Finally, the angular diagrams $\mathcal{I}(\theta,\varphi)|_{\alpha,z=z_{\text{obj}}}$ are obtained using symmetry [Eq. (44)] and angular dependence [Eqs. (37)–(39)]. A dramatic increase in calculation speed (∼30-fold) was achieved using GPU calculations with the Accelereyes plug-in for MATLAB, which resulted in a calculation time of about 3 h for a given parameter set [34 integrals over $64 \times 64 \times 256$ focal volume arrays for a 64×64 (n_x, n_y) mesh, at 80 depths].

D. Results: Angular radiation diagrams

The results of our numerical calculations of the angular intensity distribution $\mathcal{I}(\theta,\varphi)$ of SHG radiation are shown in Fig. 7 for the different sets of tendon optical parameters. All the diagrams were calculated within a forward-directed cone of 81° aperture, which is equivalent to $\mathcal{A} = n_o \sin 81° \approx 1.48$. These SHG radiation diagrams are displayed for three different polarization angles $\alpha = 0$ (a),(d), $\alpha = \pi/4$ (b),(e), and $\alpha = \pi/2$ (c),(f), and for two different imaging depths $z_{\text{obj},1} = 6\mu$m and $z_{\text{obj},2} = 30\mu$m or 27 μm. $z_{\text{obj},2}$ corresponds to the depth where a π phase shift between $(E^{\omega}_x)^2$ and $(E^{\omega}_x)^2$ is attained, which results in extinction of the induced x polarization $P^{(2\omega)}_x$ for a certain α. This depth is 30 μm for $n_o = 1.33$ and 27 μm for $n_o = 1.5$, as given by Fig. 3(e) in Sec. III

The diagrams for $\Delta n = 0$ and for the water-matched index $n = 1.33$ (a1)–(f2) have fairly similar forms within a set, varying only in relative amplitude. This can be understood as follows: first, the medium is isotropic with respect to propagation, which removes the dependence on the polarization angle α, and second, the index matching removes possible dependence on the depth z_{obj}. For the nonbirefringent case of $n = 1.5$ the diagrams are slightly different at different depths [(a3)–(c4) compared to (d3)–(f4)], which is due to spherical aberrations altering the focal field distribution.

While diagrams for the nondispersive case (a1)–(f1),(a3)–(f3) present strong forward emission with a maximum along $\theta = 0$, the diagrams for 5% dispersion have additional annular

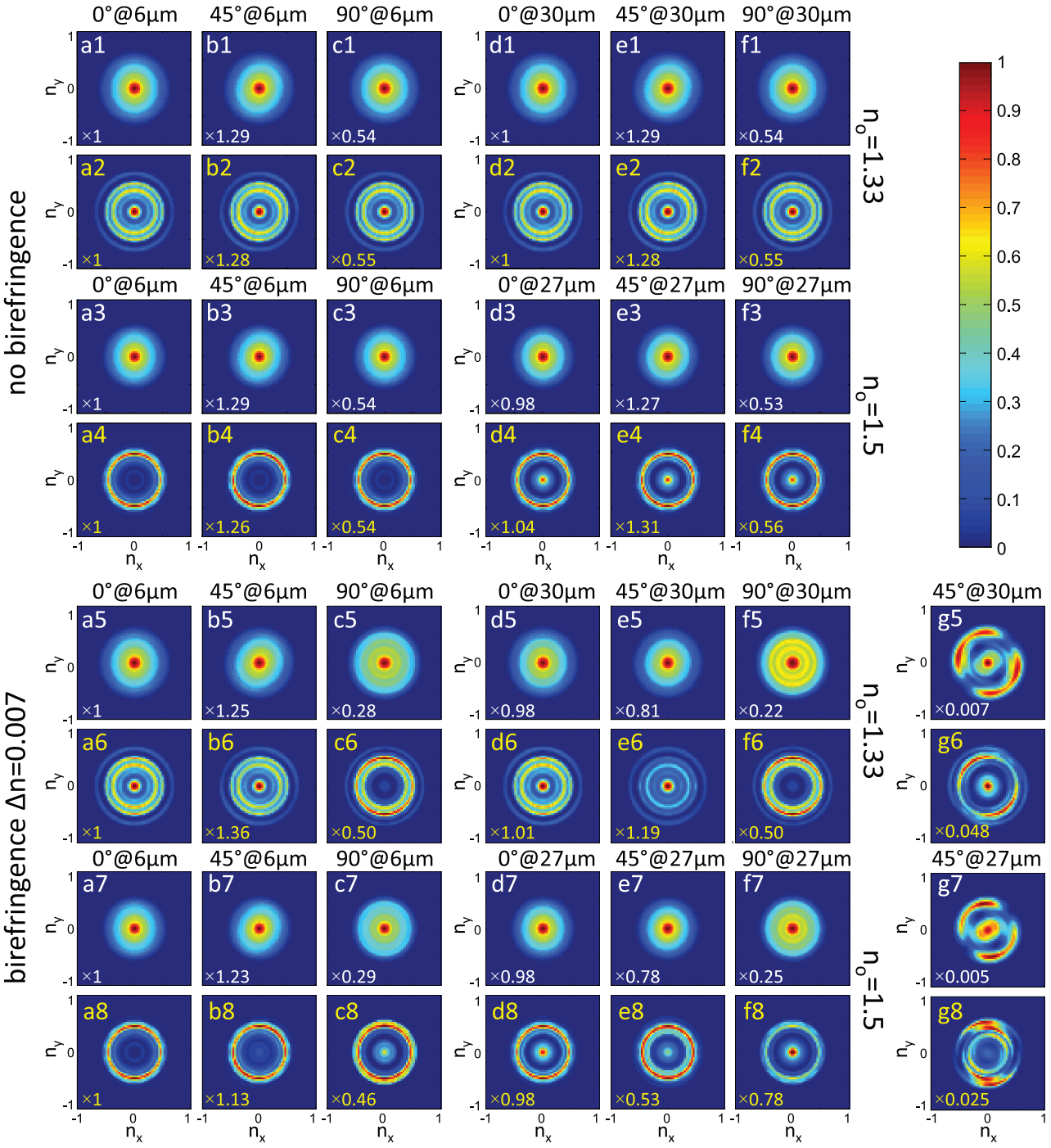

FIG. 7. (Color online) Simulated SHG radiation angular diagrams $\mathcal{I}(n_x,n_y)$ as functions of $n_x = \sin\theta\cos\varphi$ and $n_y = \sin\theta\sin\varphi$ for the eight parameter sets listed in Table I and for two different imaging depths $z_{\mathrm{obj},1}$ and $z_{\mathrm{obj},2}$. $z_{\mathrm{obj},1}$ was set to 6 μm and corresponds to the imaging plane in the proximity of the tendon-water interface. $z_{\mathrm{obj},2}$ corresponds to the depth where the phase shift between the incident squared fields $(E_x^{\omega})^2$ and $(E_y^{\omega})^2$ attains π: 30 μm for $n_o = 1.33$ and 27 μm for $n_o = 1.5$. Intensities within a set (a)–(g) are normalized to the maximal intensity in (a), and relative intensities are shown in the bottom left corner as a multiplying coefficient ($\times\cdots$). Diagrams (a) are for the incident field polarized at $\alpha = 0$ to the tendon axis, at the depth $z_{\mathrm{obj},1}$, (b) for $\alpha = \pi/4$, $z_{\mathrm{obj},1}$, (c) for $\alpha = \pi/2$, $z_{\mathrm{obj},1}$, (d) for $\alpha = 0$, $z_{\mathrm{obj},2}$, (e) for $\alpha = \pi/4$, $z_{\mathrm{obj},2}$, and (f) for $\alpha = \pi/2$, $z_{\mathrm{obj},2}$. (g) Radiation diagrams created by $P_x^{2\omega}$ at $z_{\mathrm{obj},2}$ at the angle α for which maximal intensity extinction is obtained (α shown at the upper right corner). These diagrams (g) are not observed directly.

parts (a2)–(f2) or consist exclusively of a conical lobe (a4)–(c4) with possibly a central lobe (d4)–(f4). Indeed, for the nondispersive case, the incident beam and generated SH beam are phase matched for the forward radiation, while dispersion changes the phase-matching conditions and hence the polar angle of the optimal SH radiation.

The angular diagrams for sets with birefringence $\Delta n = 0.007$ (a5)–(f8) vary considerably within a single set and

are more complex than those for $\Delta n = 0$. For a given depth and index and without dispersion, the diagrams for $\alpha = 0$ and $\alpha = \pi/2$ have slightly different forms [(a5) compared to (c5), (d5) to (f5), (a7) to (c7), (d7) to (f7)]. While the $\alpha = 0$ diagrams have a wide central lobe, the $\alpha = \pi/2$ diagrams show additional rings which are particularly neat in (f5). As one can see from the Eq. (3), the incident field polarized at both $\alpha = 0$ and $\alpha = \pi/2$ induces exclusively the $P_x^{(2\omega)}$ term. The wave it radiates is an extraordinary wave, while the incident waves for $\alpha = 0$ and $\alpha = \pi/2$ are extraordinary and ordinary waves, respectively. Thus, a particular phase matching between an incident ordinary beam and an induced extraordinary SH wave creates annular modulations of the radiation intensity. This effect is more pronounced for $n_o = 1.33$ and for the larger depth. The complex structure of diagrams for dispersive sets makes their interpretation more difficult. Quantitatively, the effect of birefringence is observed by comparing the maximal intensity on a diagram (the number in the corner) for $\alpha = \pi/4$ between $z_{\mathrm{obj},1}$ and $z_{\mathrm{obj},2}$. Indeed, while the pairs (a),(d) and (c),(f) have approximately the same intensity, (b) and (e) differ significantly. It is explained by the extinction of the $P_x^{(2\omega)}$ term due to birefringence.

Diagrams (g5)–(g8) in Fig. 7 represent the x-polarized SH intensity when the $P_x^{(2\omega)}$ term is most efficiently extinguished. It happens for a certain α when the terms $\rho E_0 \cos^2\alpha$ and $E_0 \sin^2\alpha$ are perfectly balanced. This angle α is shown in the upper right corner of diagrams. These angular diagrams are relatively irregular because they result from the residual dipole distribution produced by the difference of almost identical focal fields.

Note that for most of the parameter sets, a collection NA equal to the excitation NA ($\mathcal{A} = 0.95$) is sufficient to collect all radiated light. The only exceptions are the dispersive cases for $n_0 = 1.33$, where the faint outer ring lies beyond this aperture and requires $\mathcal{A} \approx 1.05$ to be collected.

E. Results: Total SHG intensity polarization diagrams

In this section, we present z diagrams of total SHG intensity $I(\alpha, z_{\mathrm{obj}}) = \iint \mathcal{I} d\Omega|_{\alpha, z_{\mathrm{obj}}}$. These numerical simulations of the radiated SHG intensity in the tendon were performed to test the applicability of the phenomenological model of [9] for the case of tight focusing in a birefringent medium. To that end, we applied our phenomenological model Eq. (4) to the simulation results in the same way as it was applied to the experimental data.

Figure 8 shows the numerical simulation of the total SHG intensity and parameters extracted from the simulated data according to the phenomenological model. The results are provided for the eight parameter sets listed in Table I. Simulated forward-emitted SHG intensities as functions of polarization angle α and scanning depth z_{obj} are shown in subfigures (a1)–[(a8). Subfigures (b1)–(b8) show depth intensity profiles for incident polarization angles $\alpha = 0$ (green dotted line), $\alpha = \pi/4$ (blue dashed line), and $\alpha = \pi/2$ (red dash-dotted line). Lines corresponding to these profiles are shown on the intensity diagram (a1). Subfigures (c1)–(c8) show the parameters ρ and Δ as extracted by fitting with the phenomenological model.

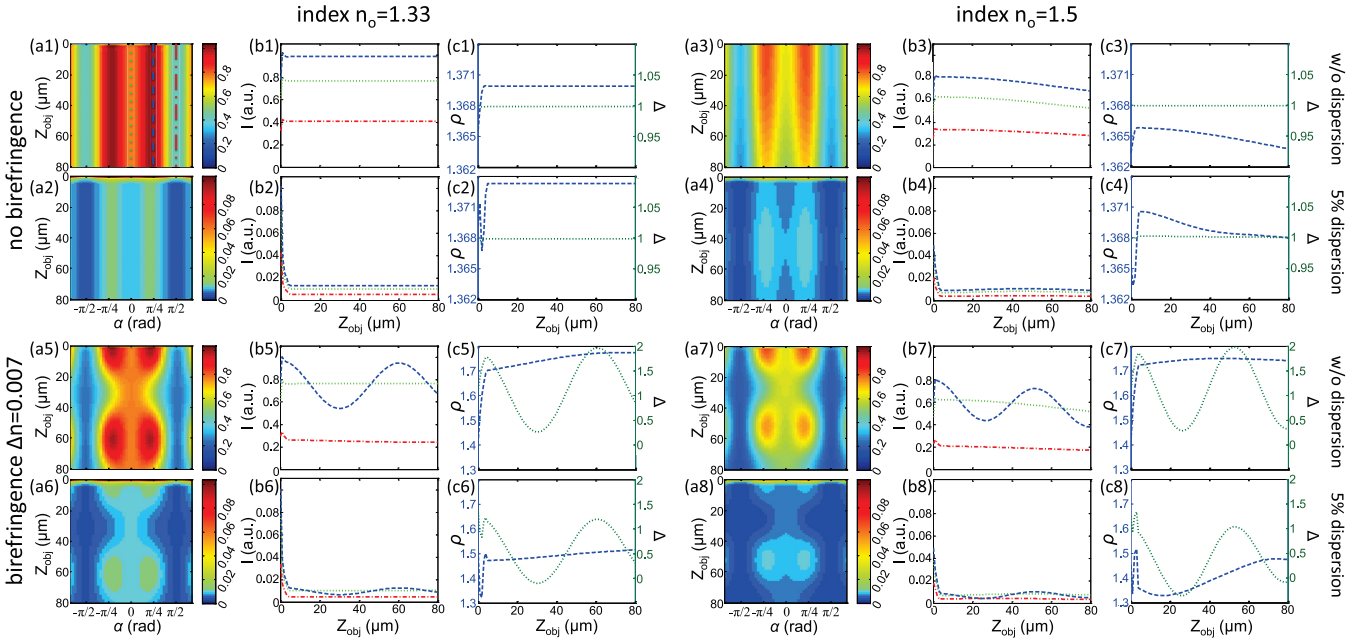

FIG. 8. (Color online) Simulated total SHG intensity in the tendon as a function of incident polarization angle α to the tendon axis and of imaging depth z_{obj} for the eight parameter sets listed in Table I. (a) SHG intensity $I(\alpha, z_{\mathrm{obj}})$ as a function of incident field polarization angle α and imaging depth z_{obj}. (b) SHG intensity depth profiles for $\alpha = 0$ (green dotted line), $\alpha = \pi/4$ (blue dashed line), and $\alpha = \pi/2$ (red dash-dotted line). (c) Anisotropic parameter ρ (blue dashed line) and parameter Δ (green dotted line) as functions of z_{obj}. ρ and Δ are extracted from the intensity diagrams as explained in [9]. Contrast is enhanced for images (a2), (a4), (a6), and (a8). Parameters used for the simulations were $\rho = 1.36$ and $\eta = 1$.

1. *Non-birefringent case:* $\Delta n = 0$, *sets no. 1–no. 4.*

The diagram for the nondispersive and index-matched case ($d = 0$, $n = 1.33$) (a1) shows constant intensity as a function of z_{obj} as expected, as the confinement of the focal field is well preserved at larger depths due to the water-tendon index matching. For the nondispersive case with index mismatch ($d = 0$, $n = 1.5$) (a3) a slight signal attenuation is observed with depth, as the focal volume deteriorates due to spherical aberrations. Diagrams for both dispersive cases (a2),(a4) show a peak of intensity at the water-tendon interface and a constant (a2) or slowly varying (a4) intensity as a function of depth beyond the interface. This steep intensity decrease is due to the altered phase-matching conditions within the beam, which results in destructive interference of SHG signals radiated from the frontal and rear halves of the beam. On the surface, when the SHG from the frontal half is not compensated, the resulting efficiency is much higher. The interfacial peak is up to ten times weaker than the intensities for the nondispersive cases (a1),(a3). The intensity beyond the surface is up to 100 times weaker as compared to the diagrams without dispersion.

ρ and Δ for nonbirefringent sets are shown in (c1)–(c4). The ρ values are very close to the value 1.36 used for the simulations. The small difference is probably due to the contribution of the z field, which is not taken into account in the phenomenological model. For the four cases (c1)–(c4) the parameter Δ is equal to 1 at all z_{obj}, as expected from Eq. (5) when $\Delta n = 0$.

2. *Birefringent case:* $\Delta n = 0.007$, *sets no. 5–no. 8.*

The intensity diagrams (nos. 5–8) are different from those without birefringence, notably because of visible periodic variations as a function of z_{obj}. The oscillating behavior of the intensity is evidenced on the depth intensity profiles (b5)–(b7) for incident angle $\alpha = \pi/4$ (blue dashed line) and are in good agreement with our previous experimental data [9]. A slight attenuation is observed with depth for $n_o = 1.5$ (a7) due to spherical aberrations which deteriorate the focusing. Identically to the nonbirefringent sets (nos. 1–4), the polarization diagrams for the two dispersive cases (a6),(a8) exhibit an interfacial intensity peak and much weaker SHG signal beyond the interface. According to [9,33,34], the set no. 8 is expected to reproduce the tendon optical parameters. However, our experimental data do not exhibit any intensity peak on the surface, but a smooth increase of intensity instead. We suppose this happens due to a less dense surface layer consisting of loose fibrils. In other words, the collagen density and $\chi^{(2)}$ also vary smoothly near the surface from zero to their respective values within the tendon.

The ρ and Δ parameters for birefringent sets are plotted in (c5)–(c8). Unlike the nonbirefringent cases (nos. 1–4), the values of ρ vary with depth and differ significantly from the value 1.36 used for calculations [$\sim$1.7 for (c5) and (c7), $\sim$1.5 for (c6), $\sim$1.35–1.5 for (c8)]. Additionally, the high values of Δ for (c5),(c6),(c7) cannot be explained by Eq. (5), as it predicts values less than or equal to unity. However, the oscillating behavior, which is due to the birefringence, is well reproduced. The fitting of Δ as a function of z_{obj} by a cosine function provides measured values for the birefringence, which coincide with great precision with the $\Delta n = 0.007$ used for calculation: 0.007 for (c5), 0.0071 for (c6), 0.0072 for (c7), 0.0071 for (c8) [for $n_o = 1.5$ the (c7),(c8) Δn values were corrected according to Eq. (23)].

V. DISCUSSION

Our results show that we do not retrieve the expected values for ρ and Δ when fitting our numerically simulated SHG data with the phenomenological model. We therefore have to reconsider this phenomenological model in the light of our theoretical computations.

According to Eqs. (2), (37), and (38) and using only the largest terms $E_{x\parallel}$ and $E_{y\perp}$ we can write for the induced polarization:

$$\begin{aligned} P_x^{(2\omega)} &\propto \rho E_{x\parallel}^2 \cos^2\alpha + E_{y\perp}^2 \sin^2\alpha, \\ P_y^{(2\omega)} &\propto E_{x\parallel} E_{y\perp} \sin 2\alpha. \end{aligned} \tag{45}$$

According to Eqs. (35), the total radiated intensity at a given α is written

$$\begin{aligned} I\big|_{\alpha, z_{\text{obj}}} &\propto \iint |\mathcal{P}^e|^2 d\Omega + \iint |\mathcal{P}^o|^2 d\Omega \\ &= \iint \left|\rho \mathcal{E}\mathcal{E}^e_{x\parallel,x\parallel} \cos^2\alpha + \mathcal{E}\mathcal{E}^e_{y\perp,y\perp} \sin^2\alpha\right|^2 d\Omega \\ &\quad + \iint \left|\mathcal{E}\mathcal{E}^o_{x\parallel,y\perp} \sin 2\alpha\right|^2 d\Omega. \end{aligned} \tag{46}$$

We recall that $\mathcal{E}\mathcal{E}^e_{x\parallel,x\parallel}$, for example, is the extraordinary wave radiation efficiency of the term $E^2_{x\parallel}$ [see Eqs. (40) and (41)]. The equation above is an elaborate analog of Eq. (4), with $\eta = 1$ and no diattenuation.

It was shown in the focal field simulations (Sec. III) that the $E_{x\parallel}$ and $E_{y\perp}$ components have almost identical magnitudes (see Fig. 2), and so do the terms $E^2_{x\parallel}$, $E^2_{y\perp}$, and $E_{x\parallel}E_{y\perp}$. However, it is generally not true for $\mathcal{E}\mathcal{E}^e_{x\parallel,x\parallel}$, $\mathcal{E}\mathcal{E}^e_{y\perp,y\perp}$, and $\mathcal{E}\mathcal{E}^o_{x\parallel,y\perp}$, as they correspond to different types of phase-matching conditions (see Fig. 9). Indeed, the term $\mathcal{E}\mathcal{E}^e_{x\parallel,x\parallel}$ corresponds to an extraordinary SH wave generated by two extraordinary incident waves and is classified as type 0. $\mathcal{E}\mathcal{E}^e_{y\perp,y\perp}$ corresponds to an extraordinary SH wave generated by two ordinary incident waves and is called type I. Finally, $\mathcal{E}\mathcal{E}^o_{x\parallel,y\perp}$ corresponds to an ordinary SH wave generated by one ordinary wave and one extraordinary wave and is called type II.

When comparing Eqs. (46) and (4), the apparent values ρ_{app} and η_{app} extracted with the phenomenological model are then written

$$\rho_{\text{app}} = \rho \frac{\iint \left|\mathcal{E}\mathcal{E}^e_{x\parallel,x\parallel}\right|^2 d\Omega}{\iint \left|\mathcal{E}\mathcal{E}^e_{y\perp,y\perp}\right|^2 d\Omega} = \rho r_I^0, \tag{47}$$

$$\eta_{\text{app}} = \frac{\iint \left|\mathcal{E}\mathcal{E}^o_{x\parallel,y\perp}\right|^2 d\Omega}{\iint \left|\mathcal{E}\mathcal{E}^e_{y\perp,y\perp}\right|^2 d\Omega} = r_I^{II}. \tag{48}$$

Here we introduced r_I^0 and r_I^{II}, which are relative SHG efficiencies for the different phase-matching types.

Measuring the apparent η_{app} delivers directly the relative efficiency r_I^{II} of types II and I. On the contrary, it follows from Eq. (47) that ρ cannot be measured separately from the relative efficiency r_I^0 of types 0 and I. The latter can only be estimated from simulations based on known optical parameters

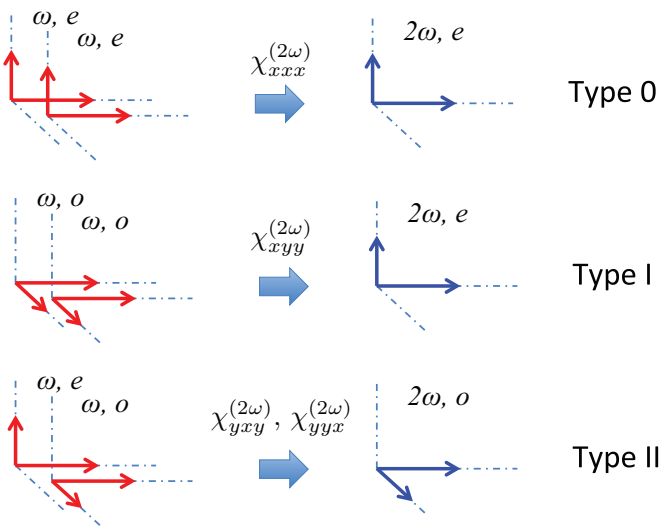

FIG. 9. (Color online) Different SHG types in the tendon by analogy with the phase-matching types in birefringent crystals. Type 0 corresponds to generation of an extraordinary wave by two extraordinary waves (governed by the $\chi^{(2\omega)}_{xxx}$ tensorial component). Type I corresponds to generation of an extraordinary wave by two ordinary waves ($\chi^{(2\omega)}_{xyy}$). Type II corresponds to generation of an ordinary wave by one extraordinary and one ordinary wave ($\chi^{(2\omega)}_{yxy}$ and $\chi^{(2\omega)}_{yyx}$).

of the tendon, but cannot be measured independently. In this case the II-to-I efficiency r_I^{II}, which can be both measured and simulated, indicates whether the optical parameters chosen for the simulation are close to their real values in tissue. Assuming that the numerical model reproduces the phase-matching behavior correctly, it also gives indications on the reliability of r_I^0 estimation from numerical simulations.

Both efficiencies r_I^0 and r_I^{II} reflect the phase matching within the focal volume, so they depend primarily on the birefringence Δn and the dispersion d, which directly influence the phase-matching conditions. For zero birefringence, both r_I^0 and r_I^{II} are unity as the ordinary and extraordinary waves experience exactly the same indices. The absolute respective efficiencies can vary upon dispersion, but this does not influence ratiometric measurements. Unity relative efficiencies result in almost exact determination of ρ and Δ from the polarization diagrams [see Figs. 8(c1)–8(c4)]. For birefringence $\Delta n = 0.007$ and for zero dispersion, for both indices we observe $\rho \sim 1.7$ and Δ up to 2 (c5),(c7), which signifies that r_I^0 is about $1.7/1.36 \approx 1.25$, and r_I^{II} is as high as $\sim$2. For both dispersive sets (c6),(c8), the measured parameters are closer to the values used for calculations, which signifies that r_I^0 and r_I^{II} are closer to 1. Finally, for the case which is expected to reproduce tendon optical parameters [see Fig. 8(c8), $\Delta n = 0.007$, $n = 1.5$, $d = 5\%$], the values of ρ_{app} and η_{app} are relatively close to the set values ($\rho = 1.36$ and $\eta = 1$).

The apparent values ρ_{app} and η_{app} obtained in the simulations have to be compared to the experimental data reported in [9,14]. Using these data, the phenomenological model provided $\eta_{\text{app}} \sim 1.2$–$1.4$ (after x and y channel calibration, not discussed in these papers), which is slightly different from that of Fig. 8(c8), but close to that of the dispersive case with $n_o = 1.33$ (c6). Even if the relative efficiencies are not explicitly related to one another, we consider that this data set no. 6, for which the simulated r_I^{II} is close to that observed in experiment, can be used to estimate r_I^0. Hence, the uncertainty on the experimentally measured ρ can also be estimated from this set. The apparent ρ_{app} in this case is 8%–10% larger than the one introduced in the calculation, and we suppose it is roughly the same for the measured ρ.

Moreover, the true values of n_o and d in the tendon may also slightly differ from those we chose for the simulation. For example, choosing smaller dispersion may result in a simulated η_{app} closer to that measured in the tendon. Testing this hypothesis would require extensive simulations to study the dependence of r_I^0 and r_I^{II} on tendon parameters, which are beyond the scope of this paper. Finally, precise independent measurements of the tendon optical parameters, such as birefringence, refractive index, and dispersion, along with simulations, would allow estimation of r_I^0 and hence the real ρ in the tendon. Note that diattenuation, while not present in the simulations, can also be accounted for in a phenomenological way using $\rho_{\text{app}} = \rho e^{-z/\Delta l_a} r_I^0$. The phenomenological model is therefore a suitable method for processing experimental data and extracting the apparent parameters (ρ_{app},η_{app}), while the numerical simulations are devoted to retrieving the real parameters (ρ,η).

One can conclude that the relative SHG radiation efficiency is a crucial property for PSHG microscopy of birefringent media. In contrast, vectorial calculations do not show strong effects of tight focusing on the PSHG signal. However, in the case of strong focusing the induced polarization $P_y^{(2\omega)}$ may contribute to the x-polarized radiated field after refocusing on the detectors, and vice versa. It thus can be a cause of the polarization scrambling reported earlier [9,14] in tendon. In order to estimate the contribution of strong focusing to this effect, we calculated the intensity detected in the x channel $I_x(\alpha, z_{\text{obj}})$ and used Eq. (4) to obtain the η parameter: $\eta = 0$ corresponds to zero scrambling, while $\eta = 1$ corresponds to a detection not resolved in polarization. For these calculations we considered two sets (nos. 3 and 4) whose effective radiation apertures are drastically different. We obtained $\eta \sim 10^{-4}$ for the narrow forward-directed emission of the set no. 3 [see Figs. 7(a3)–7(f3)] and $\eta \sim 10^{-3}$ for the wider emission with aperture of about 30° in the dispersive set no. 4 [see Figs. 7(a4)–7(f4)]. While polarization scrambling is approximately ten times larger for the field radiated in a wider cone, as expected, it is still two orders of magnitude smaller than the value $\eta \sim 0.1$ measured in tendon [9,14]. This suggests that the scrambling observed experimentally is not due to strong focusing.

VI. CONCLUSION

We performed numerical simulations of PSHG microscopy in a uniform, birefringent medium with optical index dispersion, which simulates tendon tissue. The simulation consisted first in calculating the excitation field in the medium from a high-NA objective, then calculating the induced second-order polarization, and finally calculating the SH far-field radiation. Particular attention was given to measurements of the SHG anisotropic parameter ρ in tissue.

We showed that taking into account auxiliary fields, which are absent in the low-NA limit (E_z and E_y created by an x-polarized excitation beam), had little effect on the polarization diagrams $I(\alpha, z_{\text{obj}})$ and on the measured SHG anisotropy parameter ρ. In contrast, we showed that the birefringence and the optical index dispersion affect the SHG and ρ measurements dramatically. The birefringence was partially taken into account in the previously reported phenomenological model [9], assuming the phase was constant within the focal volume. However, this work shows that the difference in focal field phase distribution between ordinary and extraordinary waves additionally changes the relative radiation efficiencies of the SHG signals. When birefringence is present, the index dispersion also has a crucial role in phase matching of various SHG contributions. To the best of our knowledge, this subtle effect of birefringence has never been observed nor discussed in the context of SHG in tissues up to now, although, it has a direct analogy with the phase-matching types for SHG in birefringent nonlinear crystals, which have been well known for decades.

Further numerical simulations of phase matching within the focal volume as a function of dispersion and birefringence should be performed to study the influence of these parameters on SHG efficiency. Additionally, precise independent measurements of tendon optical parameters such as index, dispersion, and birefringence should be performed. Nevertheless, our study already provides a comprehensive understanding of PSHG images and enables the determination of SHG anisotropy with reasonable accuracy. Moreover, as alteration of SHG efficiency due to birefringence is present as soon as the collagen assembly occupies a significant part of the focal volume, our approach applies to any collagen-rich tissues such as tendons, cornea, skin, vessels, fascia, etc. This work is therefore important for *in vivo* quantitative structural characterization of all connective tissues by use of multiphoton microscopy.

[1] S. Roth and I. Freund, J. Chem. Phys. **70**, 1637 (1979).
[2] P. Stoller, K. Reiser, P. Celliers, and A. Rubenchik, Biophys J. **82**, 3330 (2002).
[3] S. V. Plotnikov, A. Millard, P. Campagnola, and W. Mohler, Biophys. J. **90**, 693 (2006).
[4] A. Erikson, J. Örtegren, T. Hompland, C. d. L. Davies, and M. Lindgren, J. Biomed. Opt. **12**, 044002 (2007).
[5] F. Tiaho, G. Recher, and D. Rouède, Opt. Express **15**, 12286 (2007).
[6] J. C. Mansfield, C. P. Winlove, J. Moger, and S. J. Matcher, J. Biomed. Opt. **13**, 044020 (2008).
[7] S. Psilodimitrakopoulos, D. Artigas, G. Soria, I. Amat-Roldan, A. M. Planas, and P. Loza-Alvarez, Opt. Express **17**, 10168 (2009).
[8] O. Nadiarnykh and P. J. Campagnola, Opt. Express **17**, 5794 (2009).
[9] I. Gusachenko, G. Latour, and M.-C. Schanne-Klein, Opt. Express **18**, 19339 (2010).
[10] D. Aït-Belkacem, A. Gasecka, F. Munhoz, S. Brustlein, and S. Brasselet, Opt. Express **18**, 14859 (2010).
[11] J. Duboisset, D. Aït-Belkacem, M. Roche, H. Rigneault, and S. Brasselet, Phys. Rev. A **85**, 043829 (2012).
[12] A. E. Tuer, M. K. Akens, S. Krouglov, D. Sandkuijl, B. C. Wilson, C. M. Whyne, and V. Barzda, Biophys. J. **103**, 2093 (2012).
[13] P. Matteini, R. Cicchi, F. Ratto, D. Kapsokalyvas, F. Rossi, M. de Angelis, F. S. Pavone, and R. Pini, Biophys. J. **103**, 1179 (2012).
[14] I. Gusachenko, Y. Goulam Houssen, V. Tran, J.-M. Allain, and M.-C. Schanne-Klein, Biophys. J. **102**, 2220 (2012).
[15] G. Latour, I. Gusachenko, L. Kowalczuk, I. Lamarre, and M.-C. Schanne-Klein, Biomed. Opt. Express **3**, 1 (2012).
[16] A. Deniset-Besseau, J. Duboisset, E. Benichou, F. Hache, P.-F. Brevet, and M.-C. Schanne-Klein, J. Phys. Chem. B **113**, 13437 (2009).
[17] M. Rivard, M. Laliberte, A. Bertrand-Grenier, C. Harnagea, C. P. Pfeffer, M. Vallieres, Y. St-Pierre, A. Pignolet, M. A. El Khakani, and F. Legare, Biomed. Opt. Express **2**, 26 (2011).
[18] A. E. Tuer, S. Krouglov, N. Prent, R. Cisek, D. Sandkuijl, K. Yasufuku, B. C. Wilson, and V. Barzda, J. Phys. Chem. B **115**, 12759 (2011).
[19] M. Strupler, M. Hernest, C. Fligny, J.-L. Martin, P.-L. Tharaux, and M.-C. Schanne-Klein, J. Biomed. Opt. **13**, 054041 (2008).
[20] J. Mertz and L. Moreaux, Opt. Commun. **196**, 325 (2001).
[21] J. X. Cheng and X. S. Xie, J. Opt. Soc. Am. B **19**, 1604 (2002).
[22] V. V. Krishnamachari and E. O. Potma, J. Opt. Soc. Am. A **24**, 1138 (2007).
[23] N. Olivier and E. Beaurepaire, Opt. Express **16**, 14703 (2008).
[24] D. Sandkuijl, A. E. Tuer, D. Tokarz, J. E. Sipe, and V. Barzda, J. Opt. Soc. Am. B **30**, 382 (2013).
[25] M. Zimmerley, P. Mahou, D. Debarre, M.-C. Schanne-Klein, and E. Beaurepaire, Phys. Rev. X **3**, 011002 (2013).
[26] J. C. Ramella-Roman, S. A. Prahl, and S. L. Jacques, Opt. Express **13**, 10392 (2005).
[27] D. Arifler, I. Pavlova, A. Gillenwater, and R. Richards-Kortum, Biophys. J. **92**, 3260 (2007).
[28] R. Boyd, *Nonlinear Optics* (Academic Press, London, 2003).
[29] L. Novotny and B. Hecht, *Principles of Nano-Optics* (Cambridge University Press, Cambridge, 2006).
[30] S. Hacyan and R. Jáuregui, J. Opt. A: Pure Appl. Opt. **11**, 085204 (2009).
[31] P. C. Clemmow, Proc. IEE **110**, 101 (1963).
[32] P. C. Clemmow, Proc. IEE **110**, 107 (1963).
[33] N. J. Kemp, H. N. Zaatari, J. Park, H. G. Rylander, and T. E. Milner, Opt. Express **13**, 4611 (2005).
[34] A. N. Bashkatov, E. A. Genina, V. I. Kochubey, and V. V. Tuchin, SPIE Proc. **4162**, 265 (2000).
[35] M. Leutenegger, R. Rao, R. A. Leitgeb, and T. Lasser, Opt. Express **14**, 11277 (2006).